

1 This manuscript has been submitted for publication to  
2 **Geomatics, Natural Hazards and Risk**. Please note that  
3 the manuscript is under review and subsequent versions  
4 of this manuscript may have different content. If accepted,  
5 the final version of the manuscript will be available via the  
6 'Peer-reviewed Publication DOI' link on this webpage.  
7 Please feel free to contact the corresponding author.

8  
9 **Detection and forecasting of shallow landslides: lessons from a natural laboratory**

10  
11 **Rupert Bainbridge<sup>1</sup>, Michael Lim<sup>2</sup>, Stuart Dunning<sup>1</sup>, Mike G. Winter<sup>3</sup>, Alejandro Diaz-**  
12 **Moreno<sup>1,4</sup>, James Martin<sup>2</sup>, Hamdi Torun<sup>2</sup>, Bradley Sparkes<sup>5</sup>, Muhammad Khan<sup>2</sup>,**  
13 **Nanlin Jin<sup>2</sup>**

14 <sup>1</sup> Department of Geography, Newcastle University, Newcastle, NE1 7RU, UK.

15 <sup>2</sup> Faculty of Engineering and Environment, Northumbria University, Newcastle, NE1 8ST,  
16 UK.

17 <sup>3</sup> Winter Associates, Kirknewton, Midlothian, EH27 8AF, UK.

18 <sup>4</sup> Reynolds International Ltd, Broncoed Business Park, Wrexham Rd, Mold, CH7 1HP

19 <sup>5</sup> Bridgeway Consulting, Bridgeway House, Riverside Way, Nottingham NG2 1DP, UK.

20

21 Corresponding author: Rupert Bainbridge (rupert.bainbridge@newcastle.ac.uk)

22

23 **Detection and forecasting of shallow landslides: lessons from a natural laboratory**

24

25 **Rupert Bainbridge<sup>1</sup>, Michael Lim<sup>2</sup>, Stuart Dunning<sup>1</sup>, Mike G. Winter<sup>3</sup>, Alejandro Diaz-**  
26 **Moreno<sup>1,4</sup>, James Martin<sup>2</sup>, Hamdi Torun<sup>2</sup>, Bradley Sparkes<sup>5</sup>, Muhammad Khan<sup>2</sup>,**  
27 **Nanlin Jin<sup>2</sup>**

28 <sup>1</sup> Department of Geography, Newcastle University, Newcastle, NE1 7RU, UK.

29 <sup>2</sup> Faculty of Engineering and Environment, Northumbria University, Newcastle, NE1 8ST,  
30 UK.

31 <sup>3</sup> Winter Associates, Kirknewton, Midlothian, EH27 8AF, UK.

32 <sup>4</sup> Reynolds International Ltd, Broncoed Business Park, Wrexham Rd, Mold, CH7 1HP

33 <sup>5</sup> Bridgeway Consulting, Bridgeway House, Riverside Way, Nottingham NG2 1DP, UK.

34

35 Corresponding author: Rupert Bainbridge (rupert.bainbridge@newcastle.ac.uk)

36

37 **Key words: Debris flow, detection, forecasting, thresholds, monitoring**

38 **Abstract**

39         Shallow landslides are a significant hillslope erosion mechanism and limited  
40 understanding of their initiation and development results in persistent risk to infrastructure.  
41 Here, we analyse steep slopes above a strategic road, the A83 Rest and be Thankful in the west  
42 of Scotland. An inventory of 70 landslides (2003-2020) shows the development of debris flows,  
43 creep deformation and debris falls. Debris flows dominate and account for 5,350 m<sup>3</sup> (98 %) of  
44 landslide source volume. We use novel time-lapse vector tracking to detect and quantify slope  
45 instabilities, whilst seismometers demonstrate the potential for live detection and location of  
46 debris flows. Using on-slope rainfall data, we show that landslides are typically triggered by  
47 abrupt changes in the rainfall trend, characterised by high-intensity, long duration rainstorms,  
48 sometimes part of larger seasonal rainfall changes. We derive empirical antecedent  
49 precipitation (>62mm) and intensity-duration (>10 hours) thresholds over which debris flows  
50 occur. Our analysis shows the new thresholds are more effective at raising hazard alerts than  
51 the current management plan.

52         The low-cost combination of sensors provides vital information to notify of increasing  
53 hazard, the initiation of movement, and then final failure. This approach offers considerable  
54 advances to support operational decision-making for infrastructure threatened by complex slope  
55 hazards.

56 **Plain Language Summary**

57         Landslides present risks to roads, road users and economic activity. Different hillslope  
58 materials and topography determine landslide susceptibility, while weather conditions can alter  
59 the materials and the likelihood of landslides occurring, as well as directly triggering failure.  
60 These interrelated factors can limit or complicate our understanding of landslides, and makes  
61 generalisations difficult, or at least imprecise. Here we present results from low-cost local

62 monitoring that produces multiple site-specific datasets to improve the management of high-  
63 risk sites. We also present a new high resolution landslide inventory for a hillside above the  
64 A83 road in the west of Scotland. Using rainfall data, in combination with recorded landslide  
65 occurrences, we determine what rainfall conditions, both leading up to and at the point at which  
66 movement starts, generate landslides at this location. A time-lapse camera allows landslides to  
67 be timed accurately and, using computer software, we calculate changes on the slope between  
68 images to detect and monitor the early stages of movement, providing vital early warning.  
69 Finally, we use seismometers to detect when movement has occurred and to pinpoint its location  
70 on the slope. These tools can be readily deployed to monitor landslide hazards at other high-  
71 risk sites on road and rail networks, and we advocate a network of local thresholds and  
72 monitoring over regional approaches to landslide risk.

### 73 **1. Introduction**

74 Debris flows are extremely rapid ( $>5$  m/s), saturated debris-rich landslides that exist  
75 along the broad spectrum of flow-like landslides (Hungr et al., 2014). Often, shallow landslides  
76 transform into debris flows given favourable material and fluidisation conditions (e.g.  
77 Zimmerman et al., 2020). Debris flow runout potential and their capacity to entrain large  
78 quantities of water and sediment make them a significant global hazard, particularly where  
79 linear infrastructure traverses affected slopes (Geertsema et al., 2009; Meyer et al., 2015). They  
80 can be broadly grouped into channelized debris flows (CDFs) that are constrained for their flow  
81 path and hillslope (or open slope) debris flows (HDFs) that occur on non-incised slopes (Chen  
82 et al., 2009). CDFs and HDFs can transition into one another where HDFs meet gullies or CDFs  
83 breach channels and flow over slopes; it is this hillslope-gully coupling that can control the  
84 hazard potential (Milne et al., 2009). CDFs often occur in torrent systems, such as the Illgraben,  
85 Switzerland (Badoux et al., 2009), where the repeated flow path removes some of the spatial  
86 risk uncertainty and allows focussed monitoring of a single outflow channel.

87           However, at some sites historic evidence shows debris flows may occur from anywhere  
88 across wide areas with suitable topography and materials. This leads to both spatial and  
89 temporal uncertainty on triggering location and runout. At such sites, where the risk is high, a  
90 combination of active mitigation (physically controlling site aspects using barrier, net, pit, or  
91 deflection engineering infrastructure) and passive mitigation (reducing impacts via land-use  
92 planning, closures, and warning systems) methods can be used (Huebl and Fiebiger, 2005;  
93 Vagnon, 2020) but can be costly given the wide area of potential source and runout zones. In  
94 Scotland, debris flows have repeatedly damaged roads and rail lines resulting in economic and  
95 social costs (Winter et al. 2019a), with many valleys showing historic (and prehistoric) evidence  
96 of multiple debris flow deposits slope wide (Innes, 1983; Luckman, 1992; Curry, 2000).  
97 Contemporary infrastructure damaging debris flows have often been linked to high-intensity  
98 rainfall (Winter et al., 2019b). Climate forecasts suggest that in the future Scotland may receive  
99 more high intensity rainfall events in the winter and lower-frequency but higher-intensity  
100 rainfall during summer months (Finlayson, 2020; UKCP, 2018, Jones et al., 2013). Such  
101 changes in antecedent conditions and rainfall patterns may perturb hillslope sediment cascades  
102 (Bennett et al., 2014), releasing sediment from storage that is considered dormant, increasing  
103 the debris flow hazard in mountainous areas (Winter and Shearer, 2017).

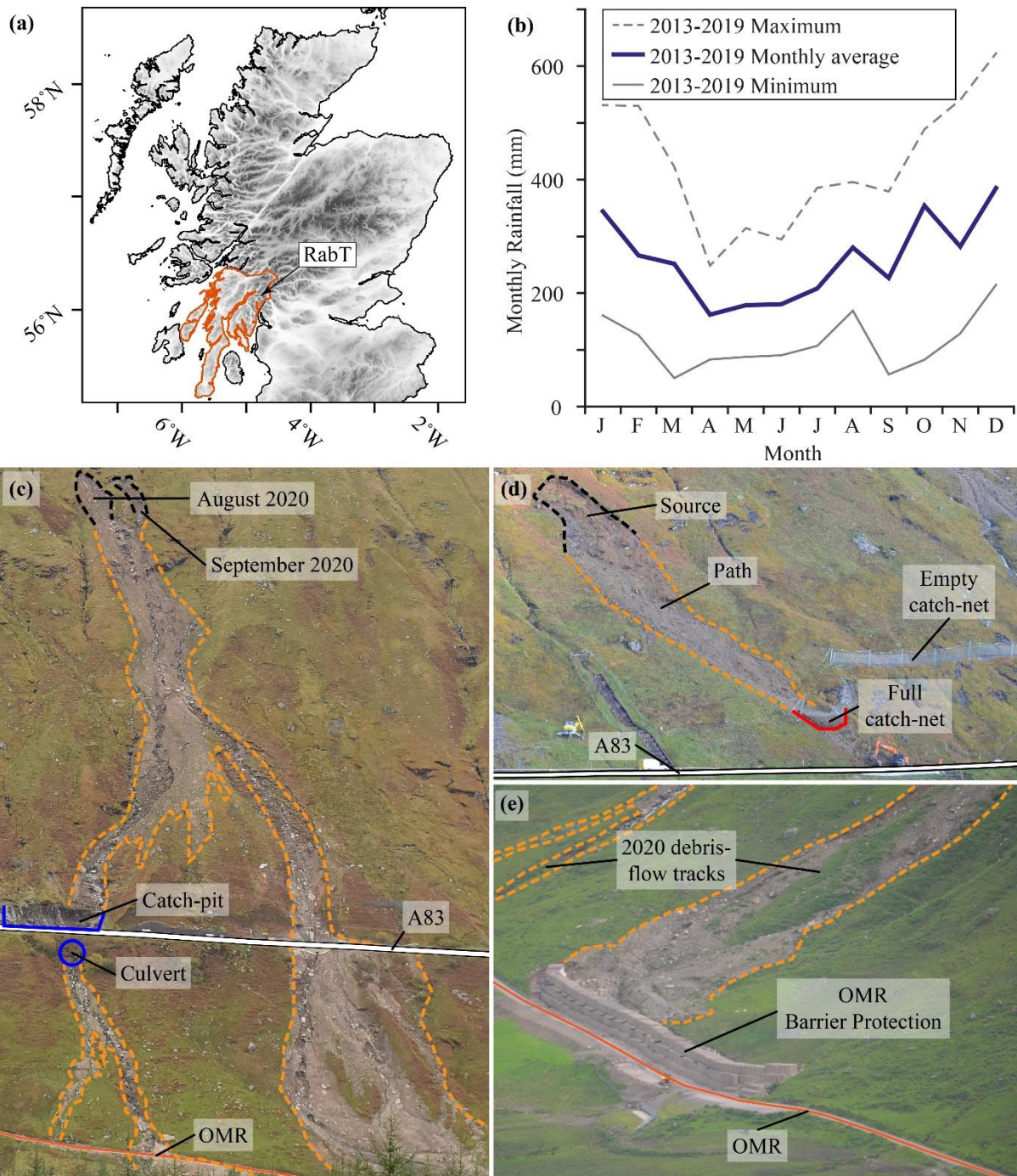
104           Monitoring strategies for determining the level of landslide hazard posed by rainfall, in  
105 a given area or slope, vary from global to hyper-local in scale. Global determination of landslide  
106 hazard requires the combination of variables such as slope, lithology, soil wetness, antecedent  
107 rainfall, and rainfall (Stanley et al. 2021). Whilst useful for global and regional indications of  
108 landslide hazard, these global models do not allow detailed analysis of areas smaller than the  
109 resolution of the data. Input data are at coarse resolution which do not always accurately  
110 represent the real-world spatial variability (Ozturk et al. 2021), making predictions noisy or  
111 imprecise. Where a higher confidence in the level of landslide hazard is required for decision

112 making at linear infrastructure for example, hyper-local monitoring can be deployed. Hyper-  
113 local monitoring collects the detail required to make site specific thresholds for landslide  
114 initiation and makes significant improvements over global landslide susceptibility models  
115 (Ozturk et al. 2021).

116 Here we demonstrate a novel combination of near-real-time, multi-disciplinary,  
117 monitoring techniques that allow remote detection and quantification of slope changes and  
118 supplement the regional Landslide Management Plan (LMP). The objective of these techniques  
119 is to improve our understanding of shallow landslide trigger mechanisms that threaten road  
120 users and infrastructure, and thus enhance alert capabilities for road asset managers at debris  
121 flow prone sites. These new, relatively low-cost, monitoring techniques and analyses are  
122 essential in helping to better manage the present and future increased risk of debris flows.

## 123 **2. Study area**

124 The A83 Rest and be Thankful (RabT), a key road into and out of west Scotland (Fig.  
125 1a), bisects the south-western slope of Beinn Luibhean upslope from Glen Croe and has the  
126 highest landslide frequency on the Scottish road network (McMillan and Holt, 2019). The  
127 average slope of the RabT is  $\sim 32^\circ$  with a relief of  $\sim 580$  m. The bedrock is Schist, with overlying  
128 glacial till up to 3 m thick, interspersed with gullies, landslide source scars, levees and lower  
129 slope debris cones (Sparkes et al., 2017, Finlayson, 2020, BGS, 2020). The surficial till deposits  
130 extend beyond the RabT site and cover much of the lower and mid-slopes of the surrounding  
131 hills in the Trossachs mountain range (BGS, 2020) where the A83 and other strategic roads  
132 route to the west and north of Scotland.



133

134 **Figure 1.** (a) Scotland digital terrain model showing the RabT location and the vulnerability  
 135 shadow for simultaneous A83/OMR road closures in orange (modified from Winter et al.  
 136 2019a). (b) RabT average monthly rainfall from 2013 to 2019 (SEPA RabT gauge; SEPA,  
 137 2020). (c) Debris flows from August and September 2020 with catch-pit and culvert mitigation.  
 138 (d) October 9<sup>th</sup> 2018 debris flow which closed the A83. The catch-net has caught the debris, but  
 139 some has exceeded the net capacity. (e) View of the OMR debris-flow protection barrier  
 140 completed in January 2021.

141

142 Average annual rainfall from 2013-2019 at the Scottish Environmental Protection  
143 Agency (SEPA) Rest and Be Thankful rainfall gauge is 3118 mm per year, with on average  
144 most rainfall occurring in October to February (Fig 1b). However, August also appears to be  
145 generally as wet as winter months and there is considerable variation in monthly rainfall  
146 between different years (Fig. 1b). The RabT is a good proxy for many sediment laden upland  
147 / mountainous systems subject to moderate to high rainfall that are susceptible to a range of  
148 slope instabilities and threaten infrastructure.

149 On average 4,000 vehicles cross the RabT per day (Winter et al. 2019a). Closures divert  
150 traffic a maximum ~88 km, if the A83 and Old Military Road (OMR; Fig. 1c), a one-way  
151 convoy diversion downslope of the A83, are closed, casting a vulnerability shadow over 4,300  
152 km<sup>2</sup> (Fig. 1a; Winter et al. 2019a). A full road closure costs ~£90k per day (2012 prices; Winter  
153 et al. 2019a) and £13.3 M has been spent on active protection of the A83, using catch-nets,  
154 catch-pits and culvert upgrades (Fig. 1c and d). This cost also includes improving the OMR to  
155 handle larger vehicles and higher traffic volumes (Scottish Parliament, 2020). However, some  
156 debris flows still exceed mitigation measures and impact the A83 and OMR. From the August  
157 2020 to January 2021 the A83 was closed for ~120 days, due to a series of large debris flows  
158 in August and September 2020 (Fig. 1c). The OMR convoy diversion was in place for much of  
159 the closure time, but additional investment was made to build a 175 m long, 6.6 m tall barrier,  
160 completed in January 2021 which protects part of the OMR from debris-flows (Fig. 1e). The  
161 barrier was installed as a response to the August-September 2020 debris-flows and a period of  
162 persistent slope creep above the A83 following those events.

163 The Scottish Road Network Landslide Study examined the full road network landslide  
164 risk and mitigation options (Winter et al., 2005). As a result, semi-quantitative and quantitative  
165 risk assessments justified additional passive mitigation measures at the RabT (Winter at al.,  
166 2009; Winter and Wong, 2020); as part of the LMP daylight patrols are dispatched and warning



167 lights activated on the RabT approach if forecast rainfall is  $\geq 25$  mm in a 24-hour period or  
168  $\geq 4$  mm in a 3-hour period (Winter et al. 2020), indicating a raised risk of debris flows.

### 169 **3. Datasets and Methodology**

#### 170 **3.1 Landslide inventories**

171 We have collated a new RabT landslide inventory from road reports (2003-2015),  
172 quarterly and event responsive terrestrial laser scans (TLS; 2015-2020) and time-lapse imagery  
173 (2017-2020). Post-2015 it is unlikely events are missing as TLS (0.1 m resolution) and time-  
174 lapse imagery data were used (Sparkes et al., 2017; Khan et al., 2021, and this study). Pre-2015,  
175 debris flows that reached the A83 are recorded, but smaller landslides and those not reaching  
176 the road may not be. The quarterly and event response TLS point cloud data were used to  
177 quantify the volume of landslide source areas using the M3C2 plugin (Lague et al., 2013) in  
178 Cloud Compare (Version 2.11.3 Anioia; <http://www.cloudcompare.org/>), which computes  
179 distances between referenced point clouds. The resulting change data were filtered to extract  
180 point-to-point losses and gains due to movement of material on the RabT slope. Longitudinal  
181 profiles of CDF and HDF source areas have been extracted from TLS point cloud derived digital  
182 elevation models (DEMs) of the RabT slope in QT Modeler (Version 8070, Applied Imagery).

#### 183 **3.2 Rainfall thresholds for landslide alerts**

184 Rainfall on seasonal, daily and 15-minute timescales are used here as indicators of  
185 increased landslide hazard at the RabT. The 2013-2019 seasonal rainfall trend was examined  
186 for the Scottish Environment Protection Agency (SEPA) RabT rain gauge data (SEPA, 2020)  
187 using the Bayesian Estimator of Abrupt change, Seasonality and Trend (BEAST) analysis  
188 package (Zhao et al., 2019). BEAST uses ensemble modelling, where multiple competing  
189 models analyse data, and Bayesian statistics derive a model average with associated  
190 probabilities that detect if seasonal and trend changes are 'true'. BEAST identifies seasonal

191 change points (SCPs) when rainfall has large inter-annual variations, i.e. the seasonal  
192 component of the rainfall time-series changes between the same time in different years. Trend  
193 change points (TCPs) are identified when the rainfall time-series trend changes abruptly. For  
194 seasonal and trend components, not all variations will lead to SCPs and TCPs being assigned,  
195 only those that have a high probability of being a genuine and significant difference, based on  
196 the agreement between competing models.

197         September to December 2018 was a particularly active landslide period at the RabT and  
198 the start of high-temporal and high-spatial resolution datasets at the site, enabling the  
199 association of debris flows to rainfall conditions. Therefore, this period is used to look in detail  
200 at rainfall conditions at and prior to debris flows.

201         We calculated the Antecedent Precipitation Index (API; Fedora and Beschta, 1989), a  
202 proxy for ground saturation (Segoni et al., 2018), for daily rainfall totals using Equation 1, as  
203 an indicator of raised debris flow hazard.

$$204 \quad API_i = k(API_{i-1}) + P_i \quad (1)$$

205         Where  $API_i$  is the API at time  $i$ ,  $P_i$  is the daily rainfall total at  $i$  and  $k$  is a constant decay  
206 function defined by the user ( $k=0.8$ ). The  $k$  value is a conservative estimate based on other  
207 works (Heggen, 2001; Viessman and Lewis 1996, Fedora and Beschta, 1989) as no stream  
208 gauge data is available for Glen Croe, so storm hydrograph regression analysis to derive a local  
209  $k$  estimate was not possible. Rainfall has been measured with an on-slope Davis Vantage Pro 2  
210 gauge (364 m a.s.l) since April 2018, better reflecting on-slope conditions than the off-slope  
211 SEPA gauge that 0.85 km away and 87 m lower in the valley.

212         Using 15-minute rainfall intensity data from the on-slope Davis Vantage Pro 2 gauge,  
213 we developed an intensity-duration (I-D) threshold over which debris flows have occurred in  
214 the past. Duration and mean rain intensity for all storms in the study period were plotted  
215 (Brunetti et al. 2010; Guzzetti et al. 2008), with a six-hour inter-event period. An I-D threshold

216 above which landslides occur was visually derived from the results (Guzzetti et al. 2008). Mean  
217 rain intensity over an entire storm was used, as opposed to mean rain intensity up to the point  
218 of the landslide, as not all landslide timings were known due to occlusion of the time lapse  
219 camera from the slope from clouds and night-time.

### 220 **3.3 Landslide initiation, tracking and detection**

221 Remote monitoring to detect slope changes can be useful for assessing slope conditions  
222 and managing infrastructure, without needing a constant personnel presence on-site. Visual  
223 analysis of imagery is useful, however an ability to analyse images pixel-by-pixel, detect  
224 changes, and quantify rates of movement provides more data to asset managers. With this ability  
225 large areas can be analysed for precursory movement before landslides occur as well as tracking  
226 and detecting movement during slope failures. Here, we process time-lapse imagery in a particle  
227 image velocimetry tool (PIVLab; Thielicke and Stamhuis, 2014; Thielicke, 2020) to detect  
228 creeping deformation on the RabT during mid- to late-September 2018, before a series of road-  
229 closing debris flows in October 2018. This time-period is used here as a good example of what  
230 this technology and these data can achieve prior to a series of large slope failures. This PIV tool  
231 has since been enhanced by Khan et al. (2021) for automatic image stabilisation, processing,  
232 and filtering. Displacement vectors and velocity were established between consecutive slope-  
233 wide images at 16x16 pixel resolution ( $\sim 2.7 \text{ m}^2$ ). Sequential deformation was derived for a  
234 point tracked through the photo sequence and inverse velocity (I-V), an analytical approach  
235 used to predict failure in brittle materials (Carlà et al., 2017), was used as an indicative metric  
236 for till failure prediction. Despite the non-brittle materials involved, some shallow landslides at  
237 the RabT appear to move as rafts of intact material over a discrete, progressively forming shear  
238 surface, and, as such have more in common with brittle failure than ductile deformation.  
239 Imminent failure is predicted when I-V values reach zero (infinite velocity), in theory, and,  
240 occasionally in practice this time can be derived from monitoring data (Fan et al. 2019; Xu et

241 al. 2020). Intervals between usable daylight images was not uniform due to cloud, rain, and  
242 night-time obscuration, so velocity data from PIVLab were interpolated to 12h intervals, with  
243 a moving average smoothing of 24h. I-V was calculated for smoothed data using  $I/(Vw)$  (e.g.  
244 Manconi and Giordan, 2016), where  $V$  is velocity over the defined time window ( $w$ ).

245 We used seismic monitoring to detect the precise timing of debris flow onset. Industry  
246 standard seismometers are used for the detection of debris flows in catchment scale torrent  
247 systems (Walter et al., 2017) and the slope failure source areas that cause them (Burtin et al.  
248 2016). Here we deploy a low-cost Raspberry Shake 3D seismometer (Raspberry Shake, 2020;  
249 Manconi et al., 2018) for directional detection of debris flows on a steep hillslope with uncertain  
250 flow initiation and routing, and short flow paths. The seismogram trace shows characteristic  
251 debris flow signals (Burtin et al. 2016), generated through clast-clast and flow-substrate  
252 interactions, above the long-term average. Conventional seismics uses cross-correlation  
253 between stations to geolocate the event generating the seismic signal (Burtin et al. 2016). Here  
254 we use hodograms (plotting signal direction through time; Borella et al., 2019) to confirm the  
255 direction of debris flow signals to the seismometer as we only had a single station deployed on  
256 the site.

#### 257 **4. Results**

258 Effective road asset management requires information on raised threats of landslide  
259 activity, significant slope changes, precursory movement and, finally, post-failure adjustment  
260 during remedial works. These data all need the context of long-term activity. This enables  
261 stakeholders to be on stand-by, pre-position resources, or proactively manage risk with targeted  
262 interventions. Here we show how the methodologies are applied to achieve alerts of high  
263 activity periods within long-term records, to quantify threshold preconditions to failure, and to  
264 create ‘event happened’ warnings that have been integrated into the management of the RabT.

265

#### 4.1 Long-term landslide activity

266

From 2003 to 2020 there were 70 landslides: 49 were debris flows (21 HDFs, 25 CDFs,

267

three of unknown type); 12 slope creep events, defined as a relatively slow gravitational

268

deformation of material; and 9 debris falls (Hungry et al. 2014), which in the case of the RabT

269

are small  $\sim 1 \text{ m}^3$  failures of surficial material, often from the top of bedrock outcrops, which do

270

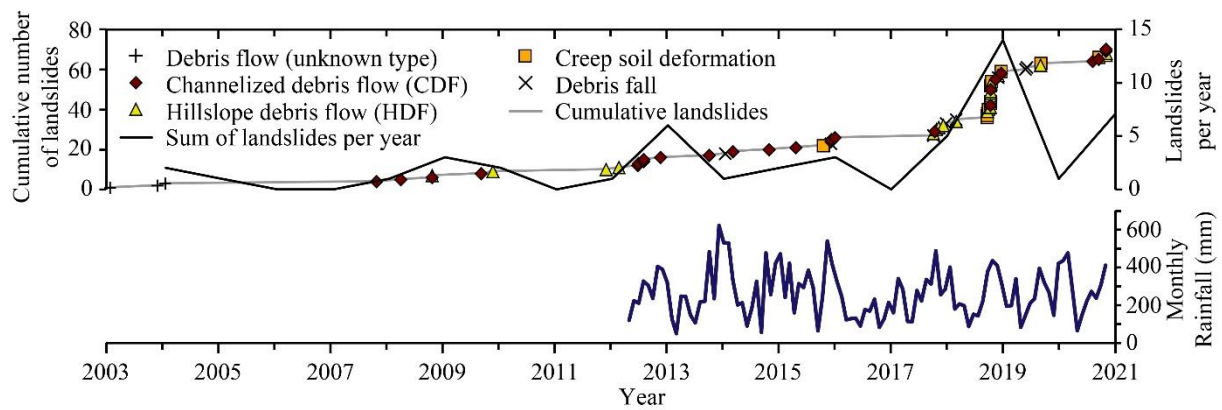
not propagate downslope (Fig. 2). Seventeen debris flows closed the A83, on average once a

271

year since 2003 though this masks the often clustered nature of events in time; eight reached

272

the OMR which requires a full diversion.



273

**Figure 2.** 2003 to 2020 cumulative landslide timeseries and yearly totals. Monthly rainfall is shown from the off-slope SEPA Rest and be Thankful gauge for the period that it is available.

275

276

63 landslides have known source locations (Fig. 3), 46% (n=29) are in till, 35% (n=22)

277

in debris cones and 19% (n=12) in regolith; 53 have volumetric information derived from TLS

278

(2015-2019) or estimates from reports (2007-2015). Thirty-six are debris flows, seven debris

279

falls and ten creep deformations. Combining the debris flows and debris falls, 18% of the

280

landslide source volume originates from the debris cones (22% of the slope by area); whilst till

281

(61% of the slope by area) and regolith (18% of the slope by area) account for 67% and 15%

282

of the landslide source volume respectively (Table 1). Creep landslide volumes were excluded

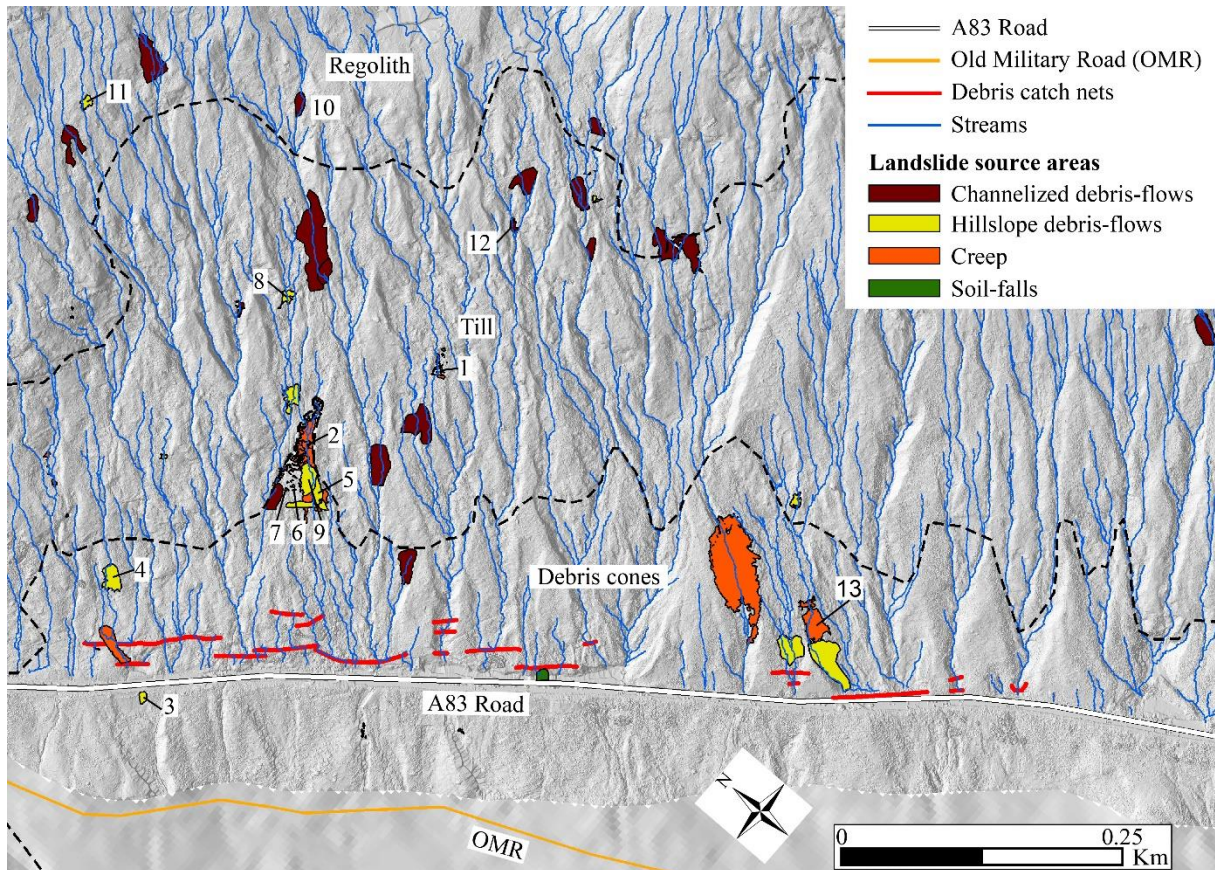
283

from the above volumetric analysis, as it is not possible to accurately measure the volume of

284

the entire moving mass from TLS data, given that much of the failed material has not been

285 evacuated from the source area. For creep landslides it is only possible to calculate the surface  
 286 volume loss. Creep landslides were found in the debris cones (n=7) and till (n=3). Most of the  
 287 surface volume loss from creep deformation occurred in the debris cones (5,673 m<sup>3</sup>) and very  
 288 little within the till (26 m<sup>3</sup>) despite its larger coverage over the slope (Fig. 3).



289  
 290 **Figure 3.** RabT landslide inventory. TLS derived hillshade and 2007 to 2019 landslide source  
 291 areas, coloured by the resulting failure type. Surface material delineation (dashed lines)  
 292 modified from Finlayson, 2020. Numbers refer to Fig. 6.

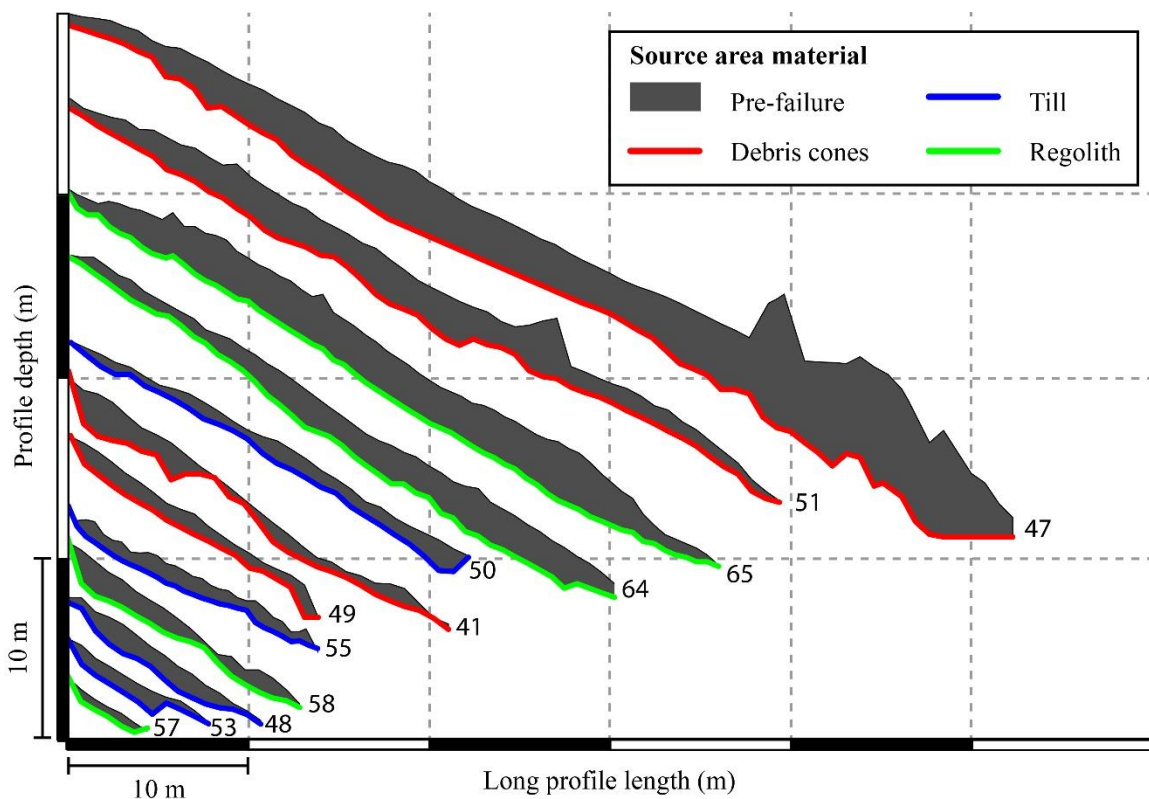
293 Volumetric contributions from different materials reflect distinct failure processes and  
 294 physical controls such as depth to bedrock. Failures originating from debris cone source areas  
 295 are generally long (15-50 m) and with the deepest recorded failures; there is a more varied  
 296 original surface-to-failure plane depth profile from debris-cone sources (Fig. 4; Table 2). Till-  
 297 based failure planes vary between 5 m and 35 m in length with a shallower depth profile  
 298 (average 1.2 m); whilst regolith failures are between 5 m to 25 m with a shallow average depth

299 profile of 0.77 m (Fig. 4). The average surface slope of the RabT is  $\sim 32^\circ$  and average failure  
 300 plane slopes for all material types range between  $30^\circ$  and  $31^\circ$ . Extrapolation of gully pathways  
 301 from a TLS derived DEM, shows a strong coupling of source areas with stream flow paths  
 302 (streams in Fig. 3).

303 **Table 1.** Summary of contribution (by area and volume) of different material source areas to  
 304 the slope failure types occurring at the site.

	Debris Cones	Till	Regolith
Number of debris flows and debris falls	11	21	11
Number of creep landslides	7	3	0
% areal slope coverage	22	61	18
% source area volume contribution	18	67	15

305



306

307 **Figure 4.** Example debris flow source area long profiles (2018-2020), derived from TLS  
 308 point clouds, showing pre- and post-failure surface elevations. Profiles are coloured by source  
 309 material type. Profiles are numbered by the landslide inventory.

310

311

**Table 2.** Descriptive statistics for the depth profiles in Figure 4.

	Inventory landslide number					
	41	47	48	49	50	51
<b>Material</b>	Debris	Debris	Till	Debris	Regolith	Debris
<b>Minimum depth</b>	0.03	0.63	0.21	0.47	0.13	0.34
<b>Maximum depth</b>	2.3	7.6	1.61	1.79	1.75	3.27
<b>Average depth</b>	0.79	3.33	0.94	0.85	0.83	1.54
<b>Standard deviation of profile depth</b>	0.62	1.82	0.43	0.32	0.34	0.7

312

**Table 2 (Cont.).** Descriptive statistics for the depth profiles in Figure 4.

	Inventory landslide number					
	53	55	57	58	64	65
<b>Material</b>	Regolith	Regolith	Till	Till	Till	Till
<b>Minimum depth</b>	0.08	0.32	0.53	0.2	0.27	0.04
<b>Maximum depth</b>	1.27	1.22	0.72	1.93	2.6	3.2
<b>Average depth</b>	0.64	0.81	0.4	1.02	1.54	2.15
<b>Standard deviation of profile depth</b>	0.04	0.24	0.74	0.49	0.61	0.79

313

314

#### 4.2 The likelihood of failure: Rainfall thresholds

315

316

317

318

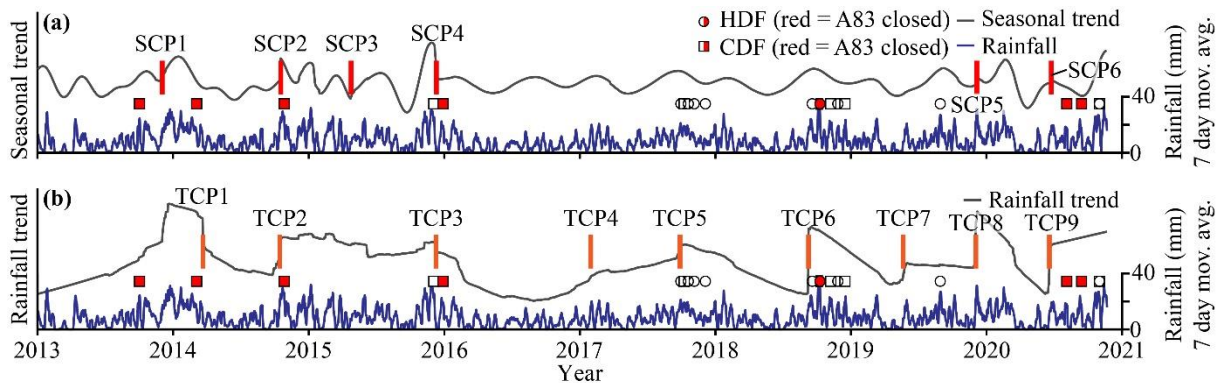
319

320

Rainfall on seasonal, daily, and 15-minute timescales has been used to indicate raised landslide hazard. BEAST identified six rainfall seasonal change points (SCP) in winter periods from 2013 to 2020 (Fig. 5a). SCP4 coincides with Storms Desmond and Frank which caused debris flows at the RabT. SCP6 in mid-2020 shortly precedes the large August-September debris flows that shut the A83. No SCPs are seen from 2016 to late-2019, but landslides do still occur. Instead, many debris flows are coincident with abrupt rainfall trend change points



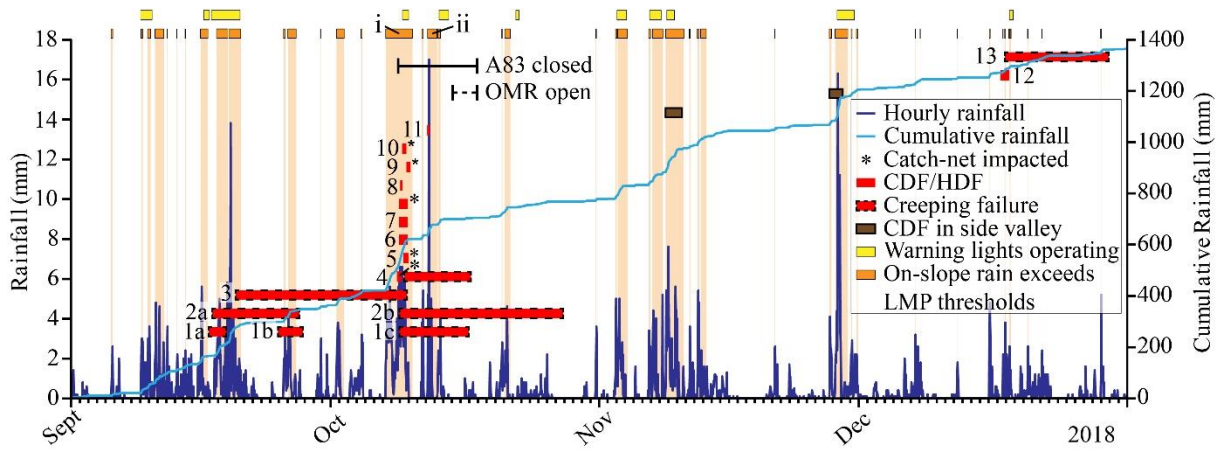
321 (TCPs) as well as their subsequent falling trends, and long period high trends (Fig. 5b). TCPs  
 322 1, 2, 3, 5, 6 and 9 are all associated with debris flow occurrence.



323  
 324 **Figure 5.** (a) BEAST seasonal rainfall component. (b) BEAST rainfall trend.

325 TCP6 starts the 2018 landslide period, a particularly active year with 19 of the 63  
 326 landslides (Fig. 2). Here we use September to December 2018, a particularly active time-period  
 327 at the RabT, as a case study to highlight the effectiveness of pro-active, near-real-time  
 328 monitoring to alert asset managers to increased landslide hazard based on rainfall thresholds,  
 329 tracking slope creep, and detecting debris flow occurrence. Time-lapse imagery has allowed  
 330 the timings of the 2018 landslides to be more accurately detected, allowing the identification of  
 331 specific rainstorms where landslides have occurred.

332 For the late-2018 period Fig. 6 shows when LMP forecast rainfall thresholds were  
 333 exceeded and warning lights were operating, along with the same thresholds plotted using on-  
 334 slope, live rain data. These data are summarized in confusion matrices which describe the  
 335 performance of the rainfall thresholds in detecting conditions that triggered landslides; data are  
 336 described as times where thresholds predict landslides will or will not happen against times  
 337 where landslides did or did not occur. False alarms and missed landslides account for 6.9% of  
 338 the study period for warning lights and 12.2% for on-slope data (Table 3).



339  
 340 **Figure 6.** 01 September to 31 December 2018 landslides, warning light activations from the  
 341 current LMP thresholds (where forecast data is used) and activations that would have occurred  
 342 using real-time on-slope data. On-slope rainfall data is from the Newcastle University Davis  
 343 gauge.

344 **Table 3.** Warning light and on-slope alert operation confusion matrix.

<i>% of study period</i>	<b>Landslide</b>		<b>No Landslide</b>	
<b>Warning lights ON / On-Slope ON</b>	<b>6.6%</b>	<b>7.7%</b>	<b>4.1%</b>	<b>11.1%</b>
<b>Warning lights OFF / On-Slope OFF</b>	<b>2.8%</b>	<b>1.1%</b>	<b>86.5%</b>	<b>80.1%</b>

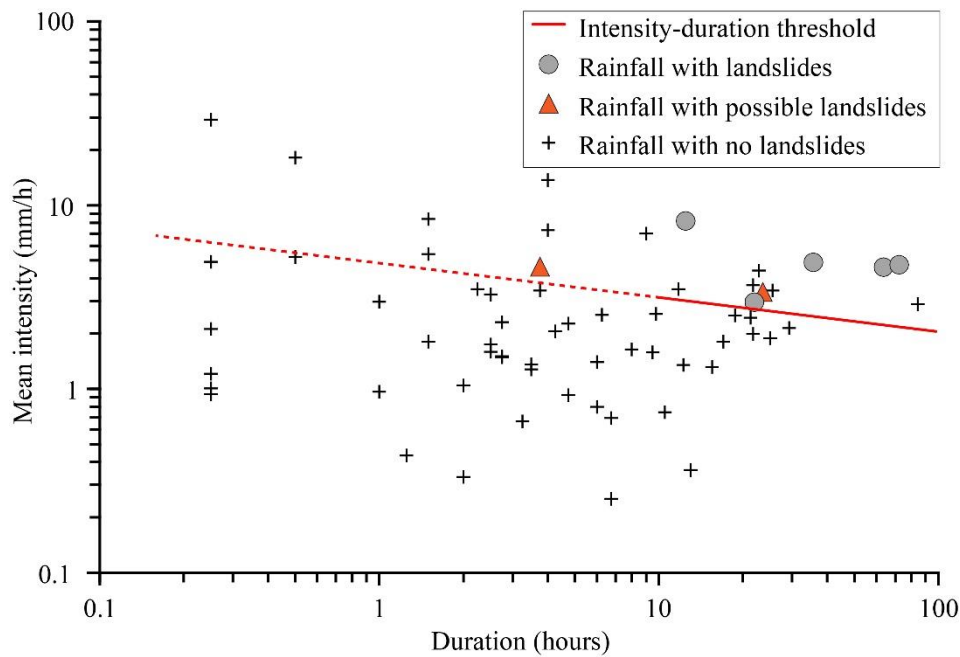
345 Warning lights are human operated, reducing false alarms through expert judgement.  
 346 However, on-slope data would raise alert levels two times where landslides occurred, that are  
 347 not fully covered by the warning lights (Fig. 6 i and ii). To improve on the current LMP rainfall  
 348 thresholds for predicting hazardous debris flow conditions on the RabT, shown in Figure 6 and  
 349 Table 3, we now look at the intensity and duration of rainstorms which generated landslides,  
 350 and antecedent precipitation.

351 Landslide producing storms in 2018 were medium (>10h) to long duration (max. 72h;  
 352 Fig. 7); however, for two storms it was not possible to determine in which the landslide  
 353 happened. Mean rain intensity for landslide initiation ranges from 2.95 mm/hr to 8.15 mm/hr.  
 354 Landslides occur above the threshold described by Equation 2.

355 
$$I = 4.75D^{-0.18} \quad (2)$$

356 Where  $I$  is mean rain intensity and  $D$  is duration. As all confirmed landslide storms were  $>10\text{h}$   
 357 duration, the threshold may not apply to  $<10\text{h}$  storms. The I-D threshold gives a false alarm for  
 358 5.7% of the study period (Table 4).

359 All landslides ( $n=18$ ) occur over an API threshold of 37 mm, with three false alarms  
 360 and long periods of alert with no landslides (Fig. 8). A 62 mm API threshold covers 90% of  
 361 landslides ( $n=16$ ), reduces false alarms to 0.8% of the study period (Table 4), but misses two  
 362 mid-December events. A combination of I-D and API thresholds maximizes landslide detection  
 363 and minimizes false alarms (Table 4). All landslide inducing storms exceed the I-D threshold  
 364 with five false alarms (Fig. 8 i to v) which API thresholds reduce to two (Fig. 8 iv, v).

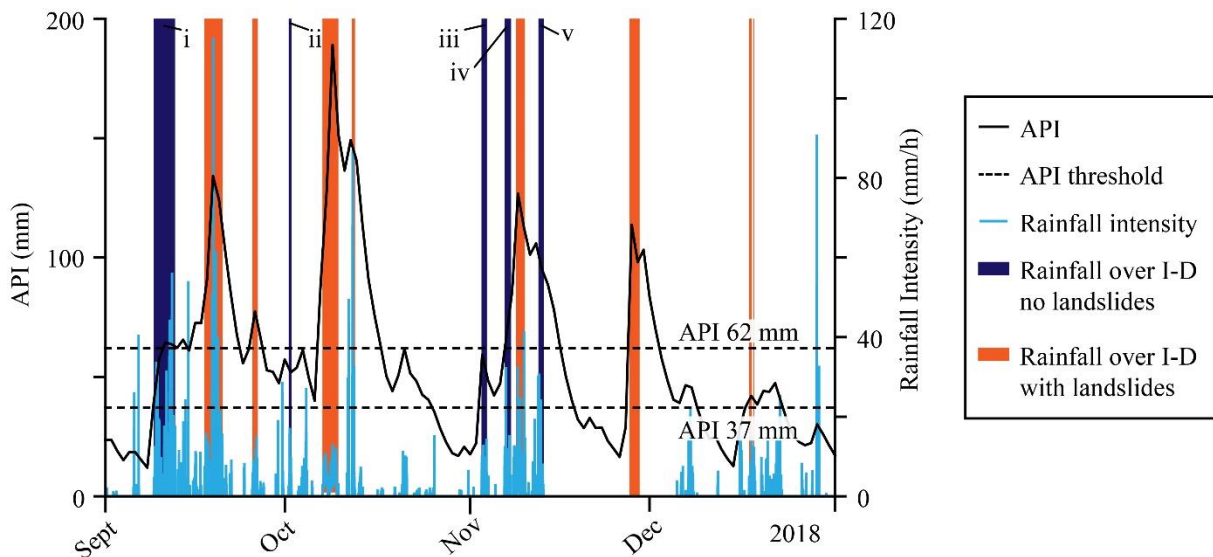


365  
 366 **Figure 7.** September to December rainstorm intensity-duration (I-D) plot.  
 367

368 **Table 4.** API and I-D threshold confusion matrix. Current LMP statistics are summarised in  
 369 Table 3.

<i>% of study period</i>	Landslide	No Landslide
<b>API &gt; threshold / I-D &gt; threshold</b>	<b>29.5%</b> 8.2%	<b>0.8%</b> 5.7%
<b>API &lt; threshold / I-D &lt; threshold</b>	<b>3.3%</b> 0.0%	<b>81.0%</b> 86.1%

370

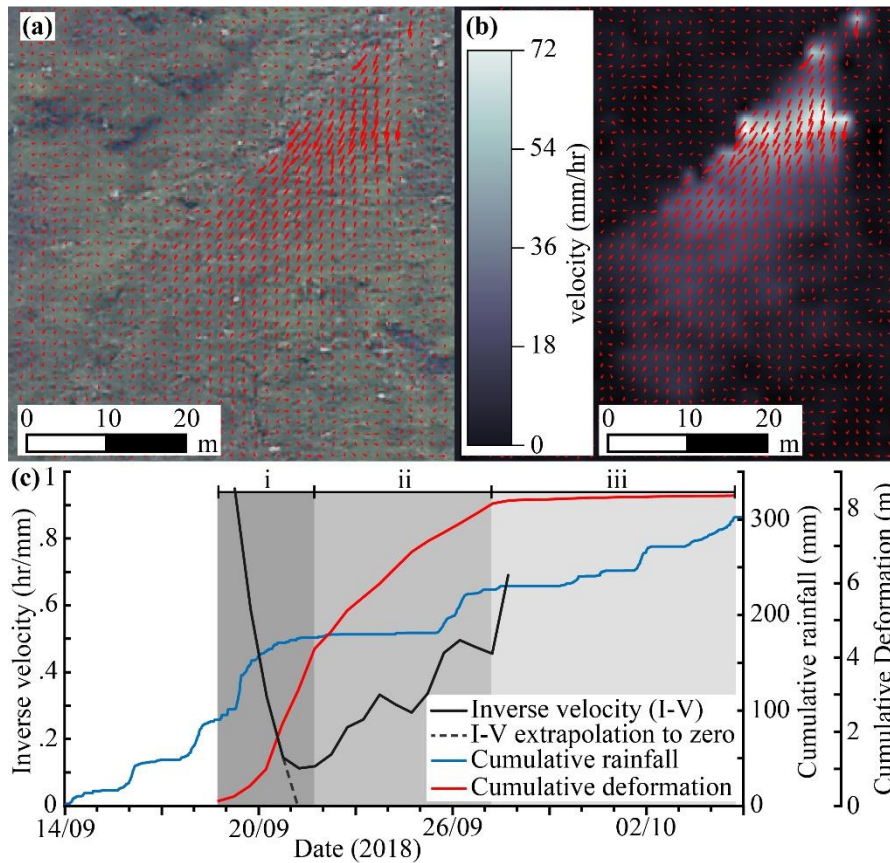


371  
 372 **Figure 8.** Antecedent Precipitation Index (API) with 37 mm and 62 mm thresholds. Rainfall  
 373 intensity (data loss 13 November to 05 December) with storms >10h duration exceeding the I-  
 374 D threshold.

375 **4.3 Early warning of slow creeping failures**

376 We monitored the creep of Failure 2 (Fig. 6) via time-lapse image vector tracking from  
 377 initiation (19 September 2018) to arrest (27 September 2018) using PIVLab (Thielicke and  
 378 Stamhuis, 2014; Thielicke, 2020; Khan et al., 2021). Vectors of change and a velocity heat map  
 379 between consecutive images are shown in Figs. 9a and 9b.

380 Creep initiation coincides with a rainstorm on the 18 September 2018 (Fig. 9c i). Half  
 381 of the total cumulative deformation occurs in the first 2.5 days. Inverse velocity (I-V) rapidly  
 382 decreases towards zero on the 19-20 September 2018; extrapolation of the I-V trend predicts  
 383 failure on the 21 September 2018. However, I-V values increase on the 21 September,  
 384 indicating reduced velocity after rainfall ceases. The deformation rate slows until arrest (Fig.  
 385 9c ii) and subsequent rainfall does not affect the deformation rate and (Fig. 9c iii).  
 386 Operationally, alert levels would be raised in Phase i when imminent failure seemed likely but  
 387 lowered in Phase ii.



388

389 **Figure 9.** (a) PIVLab deformation vector plot (Thielicke and Stamhuis, 2014). (b) Velocity heat  
 390 map. (c) Cumulative rainfall, cumulative deformation, and I-V.

391

#### 4.4 Detecting rapid debris flows

392

Seismic monitoring identified a HDF (Figs. 10a and 10b) on the 09 October 2018 and

393

located the source area. The z-axis seismogram (Fig. 10c) shows a high-amplitude signal lasting

394

~15s, corresponding with the failure time derived from time-lapse imagery, which is likely the

395

HDF in motion. Short duration, lower amplitude signals follow and are likely post-landslide

396

sediment and boulder reworking. Hodograms show very little activity at first (Fig. 10c i), but

397

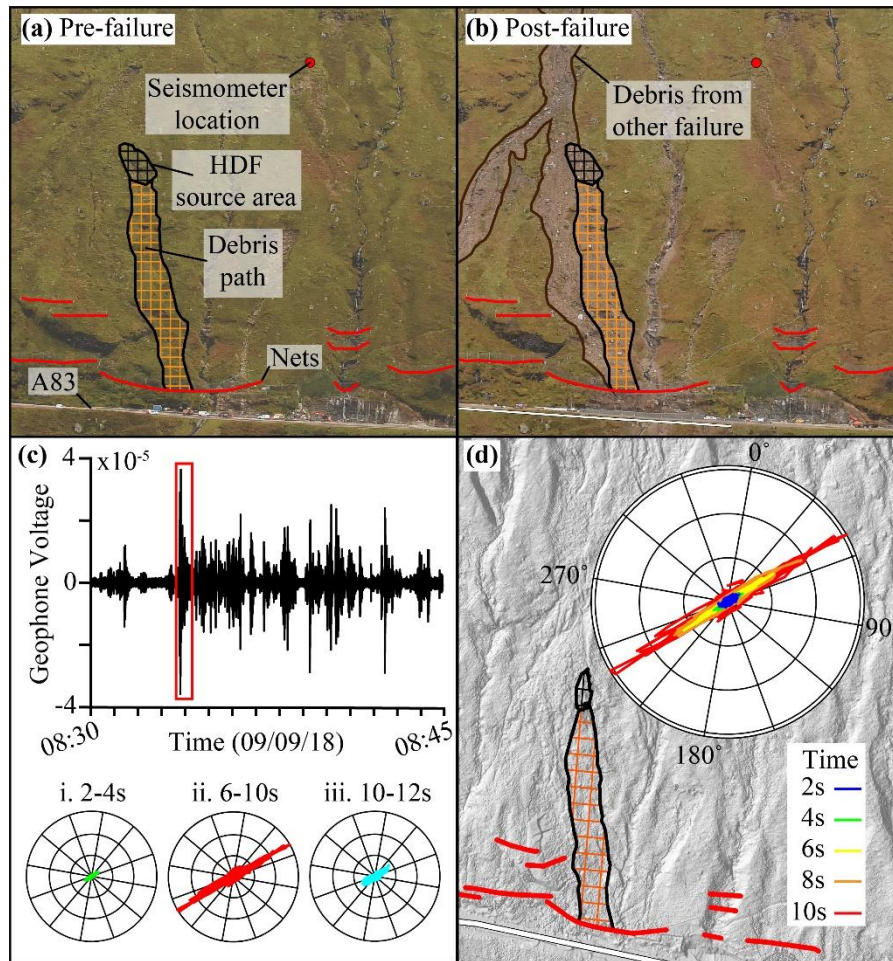
signal strength increases as the HDF signal arrives (ii) before subsiding (iii). Stacked

398

hodograms, overlain on a DEM, point to the HDF source area as the direction of the incoming

399

signal (Fig. 10d).



400

401 **Figure 10.** (a) Pre-failure HDF source and seismometer location. (b) Post-failure. (c) Fifteen-  
 402 minute seismogram with HDF signal (red box) and three hodogram time-steps (i, ii, iii). (d)  
 403 Hillshade with HDF location and ten second stacked hodogram.

404

405

406

407

408

RabT debris flow seismic signals are brief due to short, steep flow paths, with boulder and sediment reworking post-event. Another deposit on Fig. 10b, which is a thin, fine-grained drape but has a large deposit footprint, was not detected by seismic monitoring; indicating that whilst high debris content flows can be detected, hyper-concentrated flows may need larger station arrays for detection.

409

## 5. Discussion and conclusions

410

411

412

This paper presents the results of on-site monitoring at the RabT, aimed at supplementing the existing regional LMP (Winter et al., 2009). Together we show that it is possible to devise and refine thresholds for periods of likely increased landslide hazard using

413 on-slope rainfall gauges and landslide inventories with accurate timings. Further, we have  
414 shown that deformation can be detected and then tracked in near-real time, and, that final rapid  
415 failures (which many or may not have shown precursor) can be detected.

416       Between 2003 and 2020 there were 70 landslides recorded, including 49 debris flows.  
417 Landslides come from three material types on the slope: regolith, till and, debris cones, which  
418 exert a control on source area morphology and landslide volumes. Debris cone sources are  
419 generally deeper, which likely represents thicker deposits of source material to bedrock. The  
420 failure depths sourced in the upslope surface material comprising of glacial till and regolith  
421 were significantly shallower. The total volume of source areas for debris flows and debris falls  
422 across the slope is 5,404 m<sup>3</sup>, with debris cones accounting for 18% (984 m<sup>3</sup>), regolith 15% (823  
423 m<sup>3</sup>) and till the remaining 67% (3,597 m<sup>3</sup>). Each material type accounts for a proportion of  
424 source volumes similar to their areal coverage of the slope, indicating that no one material  
425 produces relatively more landslide volume than any other. However, debris cones produce  
426 fewer but larger landslides, whilst till and regolith sources produce smaller but more frequent  
427 landslides. Debris-flows in till have closed the road seven times compared to four and three  
428 times for regolith and debris cones respectively. Debris flows in till could therefore be  
429 considered as the greatest risk to road closure. Similar failure plane slope angles of 30° to 31°  
430 indicate a control on landslide initiation, which may represent a critical threshold within the  
431 slope material or relate to the dip angle of the underlying bedrock – although most failure are  
432 not at the bedrock-cover interface.

433       BEAST rainfall analysis shows that debris flows are primarily associated with abrupt  
434 rainfall trend changes, but that in some cases there is a larger seasonal signal associated with  
435 debris flow occurrence. In the 2018 study period, antecedent, and medium- to long-duration,  
436 high-intensity rainfall is shown to be an important factor in debris flows initiation. New local  
437 API and I-D rainfall thresholds, identify all landslide inducing storms and minimize false

438 alarms, improve on the LMP and provide road authorities time to consider actions. 90% of  
439 RabT landslides occurred over a 62 mm API, indicating a critical antecedent rainfall threshold.  
440 Rainstorm I-D >10h is key for landslide initiation with largely higher mean rain intensity than  
441 non-landslide storms. Whilst the thresholds have been calculated locally at the RabT, the  
442 surface geology and the topography of the site are replicated in and representative of the  
443 surrounding mountain range, indicating that the thresholds potentially apply more regionally  
444 although there is not currently a wider, timed inventory of failures.

445 Time-lapse vector tracking located and quantified creeping deformation in response to  
446 rainfall drivers. I-V calculations forecast imminent failure in the initiation phase, however creep  
447 slowed when rainfall ceased and arrested despite further rainfall. This method can detect slope  
448 movement and indicate times of heightened risk of failure for management authorities.

449 24-7 passive seismic detection and hodograms were used to identify a HDF. In this  
450 instance, and likely others due to short RabT flow paths, the 15 second event duration is too  
451 brief for live warnings but allows for 24/7 event detection and rapid response, outside of time-  
452 lapse image capture. Additional seismometers (now deployed) extend the range of detection  
453 and allow more traditional geo-location.

454 Our novel combination of sensors and processing techniques allows near-real-time  
455 monitoring and quantification of shallow landslides as demonstrated at the RabT in the west of  
456 Scotland. Results show that local sensor systems improve our understanding of triggers by  
457 allowing landslides to be attributed to specific time periods and therefore the conditions leading  
458 to their initiation are better quantified. This allows the forecasting of conditions that will likely  
459 induce landslides at the RabT, however the techniques could be readily applied to other sites.  
460 Low-cost sensors can be replicated at high- and lower-risk sites where cost-benefit would  
461 normally prevent monitoring. Increased high-intensity rainfall due to climate warming is  
462 expected in Scotland (UKCP, 2018), meaning more infrastructure and assets will have



463 increased debris flow risk. These combined low-cost monitoring techniques are an essential  
464 advancement and now operationally proven approach for addressing this future risk.

#### 465 **Acknowledgements**

466 We thank NERC (NE/P000010/1, NE/T00567X/1, NE/T005653/1), Research England  
467 ([www.Pitch-in.ac.uk](http://www.Pitch-in.ac.uk) ‘SlopeRIoT’), Transport Scotland and the Scottish Road Research Board  
468 (SRRB) for funding. We also thank BEAR Scotland, GeoRope, Jacobs, Forestry and Land  
469 Scotland, Glencroe Farm and John Mather for research, access, and on-site support. Datasets  
470 for this research are available from the Newcastle University Data Repository  
471 (<https://figshare.com/s/058074e7a14320a994ce>). We declare no conflicts of interest.

#### 472 **References**

- 473 Badoux, A., Graf, C., Rhyner, J., Kuntner, R. and McArdell, B.W. (2009). A debris-flow  
474 alarm system for the Alpine Illgraben catchment: design and performance. *Natural Hazards*,  
475 *49*, 517-539, <https://doi.org/10.1007/s11069-008-9303-x>
- 476 Bennett, G.L., Molnar, P., McArdell, B.W. and Burlando, P. (2014). A probabilistic sediment  
477 cascade model of sediment transfer in the Illgraben. *Water Resources Research*, *50*, 1225-  
478 1244, <https://doi.org/10.1002/2013WR013806>
- 479 BGS (2020). Onshore GeoIndex, <https://mapapps2.bgs.ac.uk/geoindex/home.html> (accessed  
480 June 2020)
- 481 Borella, J., Quigley, M., Krauss, Z., Lincoln, K., Attanayake, J., Stamp, L. et al. (2019).  
482 Geologic and geomorphic controls on rockfall hazard: how well do past rockfalls predict  
483 future distributions? *Natural Hazards and Earth System Sciences*, *19*, 2249–2280,  
484 <https://doi.org/10.5194/nhess-19-2249-2019>
- 485 Brunetti M.T., Peruccacci, S., Rossi, M., Luciani, S., Valigi, D. and Guzzetti, F. (2010).  
486 Rainfall thresholds for the possible occurrence of landslides in Italy. *Natural Hazards and*  
487 *Earth Systems Science*, *10*, 447-458. <https://doi.org/10.5194/nhess-10-447-2010>
- 488 Burtin, A., Hovius, N., McArdell, B. W., Turowski, J. M., and Vergne, J. (2016). Seismic  
489 constraints on dynamic links between geomorphic processes and routing of sediment in a

490 steep mountain catchment, *Earth Surface Dynamics*, 2, 21–33, <https://doi.org/10.5194/esurf->  
491 2-21-2014

492 Carlà, T., Intrieri, E., Di Traglia, F., Nolesini, T., Gigli, G and Casagli, N. (2017). Guidelines  
493 on the use of inverse velocity method as a tool for setting alarm thresholds and forecasting  
494 landslides and structure collapses. *Landslides*, 14, 517-534. <https://doi.org/10.1007/s10346->  
495 016-0731-5

496 Chen, J-C., Lin, C-W., and Wang, L-C. (2009). Geomorphic Characteristics of Hillslope and  
497 Channelized Debris Flows: A Case Study in the Shitou Area of Central Taiwan. *Journal of*  
498 *Mountain Science*, 6, 266-273. <https://doi.org/10.1007/s11629-009-0250-0>

499 Curry, A.M. (2000). Holocene reworking of drift-mantled hillslopes in the Scottish  
500 Highlands. *Journal of Quaternary Science*, 15, 529–541.  
501 <https://doi.org/10.1191/095968300666146993>

502 Fan, X., Xu, Q., Liu, J., Siva Subramanian, S., He, C., Zhu, X. and Zhou, L. (2019).  
503 Successful early warning and emergency response of a disastrous rockslide in Guizhou  
504 province, China. *Landslides*, 16, 2445–2457. <https://doi.org/10.1007/s10346-019-01269-6>

505 Fedora, M.A. and Beschta, R.L. (1989). Storm runoff simulation using an Antecedent  
506 Precipitation Index (API) model. *Journal of Hydrology*, 112, 121-133.  
507 [https://doi.org/10.1016/0022-1694\(89\)90184-4](https://doi.org/10.1016/0022-1694(89)90184-4)

508 Finlayson, A. (2020). Glacial conditioning and paraglacial sediment reworking in Glen Croe  
509 (the Rest and be Thankful), western Scotland. *Proceedings of the Geologists' Association*,  
510 131(2), 138-154. <https://doi.org/10.1016/j.pgeola.2020.02.007>

511 Gertseema, M., Schwab, J.W., Blais-Stevens, A. and Sakals, M.E. (2009). Landslides  
512 impacting linear infrastructure in west central British Columbia. *Natural Hazards*, 48, 59-72.  
513 <https://doi.org/10.1007/s11069-008-9248-0>

514 Guzzetti, F., Peruccacci, S., Rossi, M. and Stark, C.P. (2008). The rainfall intensity–duration  
515 control of shallow landslides and debris flows: an update. *Landslides*, 5, 3-17.  
516 <https://doi.org/10.1007/s10346-007-0112-1>

517 Heggen, R.J. (2001) Normalized antecedent precipitation index, *Journal of Hydrologic*  
518 *Engineering*, 6, 377-381. [https://doi.org/10.1061/\(ASCE\)1084-0699\(2001\)6:5\(377\)](https://doi.org/10.1061/(ASCE)1084-0699(2001)6:5(377))

519 Huebl, J. and Fiebigler, G. (2005). Debris-flow mitigation measures, in Jakob, M. and Hungr,  
520 O., eds., *Debris-flow Hazards and Related Phenomena*, 445-487. Springer, Berlin Heidelberg

521 Hungr, O., Leroueil, S. and Picarelli, L. (2014). The Varnes classification of landslide types,  
522 an update. *Landslides*, 11, 167-194. <https://doi.org/10.1007/s10346-013-0436-y>

523 Innes, J.L. (1983). Lichenometric dating of debris-flow deposits in the Scottish Highlands.  
524 *Earth Surface Processes and Landforms*, 8, 579-588. <https://doi.org/10.1002/esp.3290080609>

525 Jones, M.R., Fowler, H.J., Kilsby, C.G. and Blenkinsop, S. (2013). An assessment of changes  
526 in seasonal and annual extreme rainfall in the UK between 1961 and 2009: *International*  
527 *Journal of Climatology*, 33, p. 1178-1194, <https://doi.org/10.1002/joc.3503>

528 Khan, M.W., Dunning, S., Bainbridge, R., Martin, J., et al. (2021). Low-Cost Automatic  
529 Slope Monitoring Using Vector Tracking Analyses on Live-Streamed Time-Lapse Imagery,  
530 *Remote Sensing*, 13(5), 893, <https://doi.org/10.3390/rs13050893>

531 Lague, D., Brodu, N. and Leroux, J. (2013). Accurate 3D comparison of complex topography  
532 with terrestrial laser scanner: Application to the Rangitikei canyon (N-Z), *ISPRS Journal of*  
533 *Photogrammetry and Remote Sensing*, 82, 10-26,  
534 <https://doi.org/10.1016/j.isprsjprs.2013.04.009>

535 Luckman, B.H. (1992). Debris Flows and Snow Avalanche Landforms in the Lairig Ghru,  
536 Cairngorm Mountains, Scotland. *Geografiska Annaler: Series A, Physical Geography*, 74:2-  
537 3, 109-121, <https://doi.org/10.1080/04353676.1992.11880355>

538 Manconi, A., Coviello, V., Galletti, M. and Seifert, R. (2018). Short Communication:  
539 Monitoring rockfalls with the Raspberry Shake. *Earth Surface Dynamics*, 6, 1219-1227.  
540 <https://doi.org/10.5194/esurf-6-1219-2018>

541 Manconi, A. and Giordan, D. (2016). Landslide failure forecast in near-real-time. *Geomatics,*  
542 *Natural Hazards and Risk*, 7:2, 639-648. <https://doi.org/10.1080/19475705.2014.942388>

543 Meyer, N., Schwanghart, W., Korup, O. and Nadim, F. (2015). Roads at risk: traffic detours  
544 from debris flows in southern Norway. *Natural Hazards and Earth System Science*, 15, 985-  
545 995. <https://doi.org/10.5194/nhess-15-985-2015>

546 McMillan, F.N. and Holt, C.A. (2018). BEAR Scotland NW trunk road maintenance: efficient  
547 management of geotechnical emergencies. *Quarterly Journal of Engineering Geology and*  
548 *Hydrogeology*, 52, 286-294. <https://doi.org/10.1144/qjegh2018-035>

549 Milne, F.D., Werritty, A., Davies, M.C.R. and Brown, M.J. (2009). A recent debris flow event  
550 and implications for hazard Management. *Quarterly Journal of Engineering Geology and*  
551 *Hydrogeology*, 42, 51–60. <https://doi.org/10.1144/1470-9236/07-073>

552 Ozturk, U., Saito, H., Matsushi, Y., Crisologo, I. and Schwanghart, W. (2021) Can global  
553 rainfall estimates (satellite and reanalysis) aid landslide hindcasting?. *Landslides*,  
554 <https://doi.org/10.1007/s10346-021-01689-3>

555 Raspberry Shake (2020). <https://raspberrysshake.org/> (accessed June 2020)

556 Scottish Parliament (2020). Official Report of the Public Petitions Committee, 05 March  
557 2020. <http://www.parliament.scot/parliamentarybusiness/report.aspx?r=12561> (accessed, July  
558 2020)

559 Segoni, S., Rosi, A., Lagomarsino, D., Fanti, R. and Casagli, N. (2018). Brief communication:  
560 Using averaged soil moisture estimates to improve the performances of a regional-scale  
561 landslide early warning system. *Natural Hazards and Earth System Science*, 18, 807-812.  
562 <https://doi.org/10.5194/nhess-18-807-2018>

563 SEPA, (2020). Rest and Be Thankful 15-minute rainfall record.  
564 <https://www2.sepa.org.uk/rainfall/> (accessed May 2020)

565 Sparkes, B., Dunning, S., Lim, M. and Winter, M.G. (2017). Characterisation of Recent  
566 Debris Flow Activity at the Rest and Be Thankful, Scotland, in Mikoš, M., Vilímek, V., Yin,  
567 Y. and Sassa, K., eds., *Advancing Culture of Living with Landslides, Volume 5 Landslides in*  
568 *Different Environments: WLF: Workshop on World Landslide Forum Conference*  
569 *Proceedings*, 51-58. [https://doi.org/10.1007/978-3-319-53483-1\\_8](https://doi.org/10.1007/978-3-319-53483-1_8)

570 Stanley, T.A., Kirschbaum, D.B., Benz, G., Emberson, R.A., Amatya, P.M., Medwedeff, W.  
571 and Clark, M.K. (2021). Data-Driven Landslide Nowcasting at the Global Scale. *Frontiers in*  
572 *Earth Science*, 9:640043, <https://doi.org/10.3389/feart.2021.640043>

573 Thielicke, W. (2020). PIVlab - particle image velocimetry (PIV) tool.  
574 [https://www.mathworks.com/matlabcentral/fileexchange/27659-pivlab-particle-image-](https://www.mathworks.com/matlabcentral/fileexchange/27659-pivlab-particle-image-velocimetry-piv-tool)  
575 [velocimetry-piv-tool](https://www.mathworks.com/matlabcentral/fileexchange/27659-pivlab-particle-image-velocimetry-piv-tool), MATLAB Central File Exchange. (Accessed July 2020)

576 Thielicke, W. and Stamhuis, E.J. (2014). PIVlab – Towards User-friendly, Affordable and  
577 Accurate Digital Particle Image Velocimetry in MATLAB. *Journal of Open Research*  
578 *Software*, 2 (1), e30. <http://doi.org/10.5334/jors.bl>

579 UKCP. (2018). UK Climate Projections. Met Office.  
580 <https://www.metoffice.gov.uk/research/approach/collaboration/ukcp/> (accessed June 2020)

581 Vagnon, F. (2020). Design of active debris flow mitigation measures: a comprehensive  
582 analysis of existing impact models. *Landslides*, 17, 313-333. [http://doi.org/10.1007/s10346-](http://doi.org/10.1007/s10346-019-01278-5)  
583 019-01278-5

584 Viessman, W., Jr., and Lewis, G. L. (1996). Introduction to hydrology. 4th Ed.,  
585 HarperCollins, New York.

586 Walter, F., Burtin, A., McArdell, B., Hovius, N., Weder, B., Turowski, J.M. (2017). Testing  
587 seismic amplitude source location for fast debris-flow detection at Illgraben, Switzerland.  
588 Natural Hazards and Earth System Science, 17, 939-955. [https://doi.org/10.5194/nhess-17-](https://doi.org/10.5194/nhess-17-939-2017)  
589 939-2017

590 Winter M.G., Macgregor F., Shackman, L. (2009). Scottish Road Network Landslides Study:  
591 Implementation, The Scottish Executive, Edinburgh

592 Winter, M.G., Peeling, D., Palmer, D. and Peeling, J. (2019a). Economic impacts of  
593 landslides and floods on a road network. *AUC Geographica*, 54 (2), 207-220,  
594 <https://doi.org/10.14712/23361980.2019.18>

595 Winter, M.G., Ognissanto, F. and Martin, L.A. (2019b). Rainfall Thresholds for Landslides  
596 Deterministic and Probabilistic Approaches. *Transport Research Laboratory Published*  
597 *Project Report PPR901*, <https://trl.co.uk/reports/rainfall-thresholds-landslides>

598 Winter, M.G., Kinnear, N. and Helman, S. (2020). A technical and perceptual evaluation of a  
599 novel landslide early warning system. *Proceedings, Institution of Civil Engineers (Transport)*,  
600 <https://doi.org/10.1680/jtran.19.00138>

601 Winter, M.G. and Wong, J.C.F. (2020). The assessment of quantitative risk to road users from  
602 debris flow. *Geoenvironmental Disasters*, 7(4), 1-19. [https://doi.org/10.1186/s40677-019-](https://doi.org/10.1186/s40677-019-0140-x)  
603 0140-x

604 Xu, Q., Peng, D., Zhang, S., Zhu, X., He, C., Qi, X., Zhao, K., Xiu, D. and Ju, N. (2020)  
605 Successful implementations of a real-time and intelligent early warning system for loess  
606 landslides on the Heifangtai terrace, China. *Engineering Geology*, 278.  
607 <https://doi.org/10.1016/j.enggeo.2020.105817>

608 Zhao, K., Wulder, M.A., Hu, T., Bright, R., Wu, Q., Qin, H., et al., (2019). Detecting change-  
609 point, trend, and seasonality in satellite time series data to track abrupt changes and nonlinear  
610 dynamics: A Bayesian ensemble algorithm. *Remote Sensing of Environment*, 232.  
611 <https://doi.org/10.1016/j.rse.2019.04.034>

612 Zimmerman, F., McArdell, B.W., Rickli, C. and Scheidl, C. (2020). 2D Runout Modelling of  
613 Hillslope Debris Flows, Based on Well-Documented Events in Switzerland. *Geosciences*,  
614 *10*(2):70. <https://doi.org/10.3390/geosciences10020070>